Editors' Suggestion

Analysis of Membrane Phononic Crystals with Wide Band Gaps and Low-Mass Defects

C. Reetz,[1,*] R. Fischer,[1,2] G.G.T. Assumpção,[1] D.P. McNally,[1] P.S. Burns,[1] J.C. Sankey,[3] and C.A. Regal[1]

[1] *JILA, National Institute of Standards and Technology and University of Colorado, and Department of Physics, University of Colorado, Boulder, Colorado 80309, USA*
[2] *Rafael Ltd., Haifa 31021, Israel*
[3] *Department of Physics, McGill University, Montreal, Canada*

(Received 26 June 2019; revised manuscript received 16 September 2019; published 14 October 2019)

We present techniques to model and design membrane phononic crystals with low-mass defects, optimized for force sensing. Further, we identify the importance of the phononic crystal mass contrast as it pertains to the size of acoustic band gaps and to the dissipation properties of defect modes. In particular, we quantify the tradeoff between high-mass-contrast phononic crystals, with their associated robust acoustic isolation, and a reduction of soft clamping of the defect mode. We fabricate a set of phononic crystals with a variety of defect geometries out of high-stress stoichimetric silicon-nitride membranes and measure at both room temperature and 4 K in order to characterize the dissipative pathways across a variety of geometries. Analysis of these devices highlights a number of design principles integral to the implementation of low-mass low-dissipation mechanical modes into optomechanical systems.

DOI: 10.1103/PhysRevApplied.12.044027

I. INTRODUCTION

Many nanoscale sensing and transduction protocols are based on detection of the minuscule forces between a sample and a highly sensitive probe. Examples include microscopy methods such as atomic force microscopy (AFM) and magnetic resonance force microscopy (MRFM) [1,2]. Additionally, an increasing number of quantum protocols make use of a mechanical intermediary to transduce between two types of otherwise noninteracting quantum systems [3–5]. Readout of the mechanical motion can be achieved through a range of optical, electrical, or magnetic means [6,7]. Fundamentally, all these techniques are often limited by environmental, i.e., thermal or Brownian, noise coupled to the mechanical resonator. This noise leaks into the mechanical mode at the mechanical damping rate as dictated by the fluctuation-dissipation theorem, defining a force sensitivity noise floor.

The factors that define mechanical damping to the environment have been a long-standing question. Generally, loss mechanisms can be divided into two categories: acoustic radiation into the external structure [8] and internal loss (dissipation) of acoustic motion to heat through bending—either at the clamping point or within the structure itself. Historically, control of materials has been a main driver at reducing loss. Recently, progress has increasingly been propelled by the engineering of geometry and structural parameters to mitigate both mechanisms. Silicon-nitride tensioned thin films are a platform that offer multiple control parameters [9–18]. The tension of the film results in dissipation dilution, which maintains low dissipation while increasing the oscillator energy. Acoustic isolation in the form of band-gap engineering of the surrounding substrate can control acoustic radiation [19–21] and, in recent realizations, nanopatterning of the tensioned SiN film itself can provide both (1) a phononic band gap and (2) the phenomenon called soft clamping, which describes the gradual decay of the mechanical mode into the phononic crystal (PnC) structure, reducing bending loss [17,18].

In this work, we explore PnCs with varying mass contrast and associated defect designs in two-dimensional (2D) periodic structures. We observe that increasing mass contrast of the PnC widens the band gap in the frequency domain [Figs. 1(a) and 1(b)]; at the outset, this improves isolation of the mechanical motion and avoids contamination of the spectrum due to thermal noise of the integrated motion of other modes. Further, designs with a high mass ratio are amenable to analytic analysis, as has been carried out recently in the context of one-dimensional (1D) PnC strings [18]. This design methodology simplifies the design of a range of defects, in particular, smaller effective mass defects and hence better force sensitivity. Small-mass

*christopher.reetz@colorado.edu

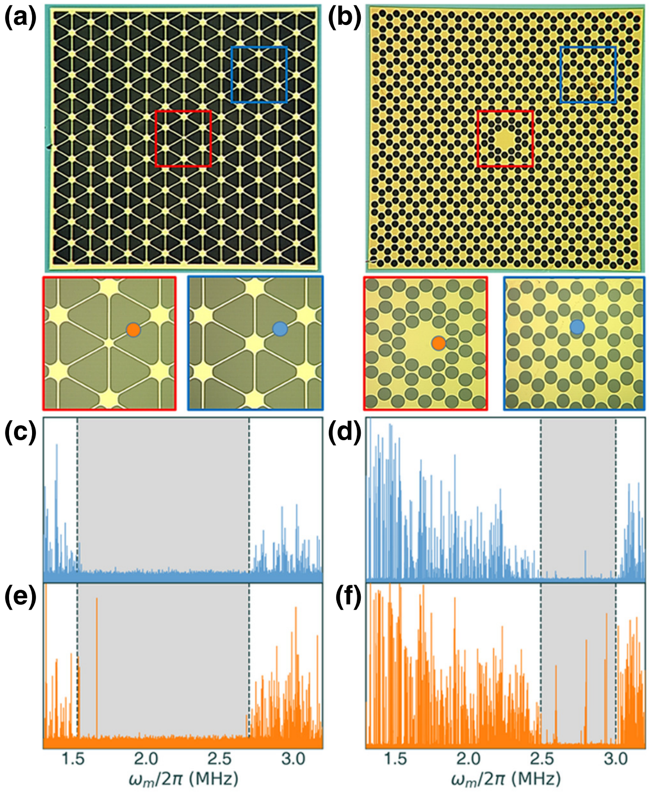

FIG. 1. (a),(b) An optical-microscope image of high- and low-mass-contrast PnC devices containing a defect respectively. The displacement of the devices measured both in the crystal bulk (blue) and at the defect (orange). (c),(e) Thermal noise spectra of the high-contrast device on a logarithmic scale. The defect mode shown in (e) is the fundamental symmetric mode. (d),(f) Mechanical spectra for the low-contrast device on a logarithmic scale. The device is driven with sufficient white noise in order to observe all expected defect modes. The spectrum shown in (f) contains five separate defect modes within the band gap, including the second symmetric mode examined in this study. The defect-mode frequencies in both (e),(f) agree with predictions from 2D FEM simulations. Mechanical modes that appear inside the band gap in (d) have quality factors less than 100, and therefore are most likely hybridized modes between the membrane and the silicon chip or mounting assembly.

defects can also be incorporated into low-contrast PnCs, through insights from finite-element method (FEM) simulations and we study a range of defect designs and measurements in low-contrast PnCs [17].

When increasing the mass contrast of PnCs, mode localization is enhanced, but a consequence is a reduction in soft clamping, which increases susceptibility to internal (bending) loss. Here, we consider this decrease in soft clamping quantitatively by examining the bending of multiple combinations of intertwined PnC and defect designs. We note that the choice of the tradeoff between localization and soft clamping will depend upon the application considered; when operating at room temperature, soft clamping is critical, but when at deeply cryogenic temperatures [13] or in crystalline materials [22,23], the associated small internal loss rates may allow for sufficiently low dissipation even when the mode is strongly localized.

For designs in this work, we specifically have in mind applications where high force sensitivity is desired for megahertz-scale membrane resonators simultaneously coupled to an optical mode and a spin or electrical degree of freedom [24–26]. For these functionalization purposes, we consider a few design constraints. These include designing defects large enough to couple to Fabry-Perot cavities [27], fabricating wide band gaps that can incorporate a wide variety of defects robust to perturbations due to deposition of metallic or magnetic components, as well as limiting device size to avoid instabilities resulting from low-frequency mechanical modes.

We begin the paper with an analytic and numerical analysis of design considerations for optimizing both bending and radiative loss. In particular, we correlate the PnC mass contrast to band-gap width, phononic isolation, and variation in mechanical quality (Q) due to corresponding changes in soft clamping. In this way, we link the geometrical design considerations needed to achieve soft clamping to a relatively narrow band gap. We then present measurements of a set of five devices with varying band gaps and defects; we study Q at both room temperature and at 4 K, where internal loss is the dominant contributor, such that we can compare the experimental results to loss prediction from bending. As a primary metric, we examine the mechanical force sensitivity of all devices, developing design principles for combinations of both low-mass and low-loss mechanical defects. We also identify structures in which nuances of defect design have deleterious consequences, such as considerable defect bending or large effective mass. In this study, we utilize 100-nm-thick SiN PnCs and demonstrate force sensitivities down to 12 aN$/\sqrt{\mathrm{Hz}}$ at temperatures of 4 K and a frequency of 1.6 MHz. We expect that thinner films and colder temperatures will further enable optomechanics that combines high-frequency membranes with excellent force sensitivity [13–15,17,28].

II. CONCEPT AND PnC MODELING

Here, we present the design and analysis of 2D PnC structures and their defects. The defect is designed such that it has one or more mechanical modes within the band gap of the surrounding PnC. Such a design supports a spatially localized mechanical mode within the larger patterned membrane structure. The design of all devices in this work is guided by an optimization of the force sensitivity [29]:

$$S_{\mathrm{FF}} = \frac{4k_B T m\omega_m}{Q} = \frac{2\hbar k_B T}{Q x_{\mathrm{zp}}^2}. \qquad (1)$$

Here, x_{zp} is the resonator's fluctuation at zero absolute temperature, ω_m is the angular frequency of the mechanical mode, T is the temperature, k_B is the Boltzmann constant, and m is the effective mass of the mode. We emphasize that the appearance of x_{zp} is not an indication of quantum effects but, rather, a convenient parametrization as x_{zp} is a fundamental parameter in both the force sensitivity and the optomechanical coupling [6]. We see that force sensitivity can be enhanced by maximizing both x_{zp} and Q. In pursuit of the latter, we note that dissipation can be expressed as a sum of two contributions:

$$\frac{1}{Q} = \frac{1}{Q_{\text{bend}}} + \frac{1}{Q_{\text{rad}}}, \tag{2}$$

where Q_{bend} arises from the internal or bending losses of the mechanical mode, while Q_{rad} encapsulates acoustic radiation that is lost to the substrate and the wider environment. A SiN PnC can enhance both Q_{rad} and Q_{bend} via acoustic isolation and soft clamping, respectively.

A. 1D model for phononic crystals

In this work, we are ultimately interested in the design and fabrication of 2D structures. However, the main design methodologies and concepts can be elucidated by considering a 1D analysis, where we convert a 2D unit cell (Fig. 2) to a 1D unit cell. In this work, we separate each unit cell into regions of thin tethers and wide pads, as depicted in Fig. 1(a). In this geometry, the pads (tethers) will have slower (faster) wave velocities than the unpatterned membrane. Periodic modulation of the wave velocity results in gaps in the acoustic spectrum. This procedure, in principle, integrates over the mass of the transverse dimension and recalculates the appropriate wave velocities. The details are outlined in Appendix A.

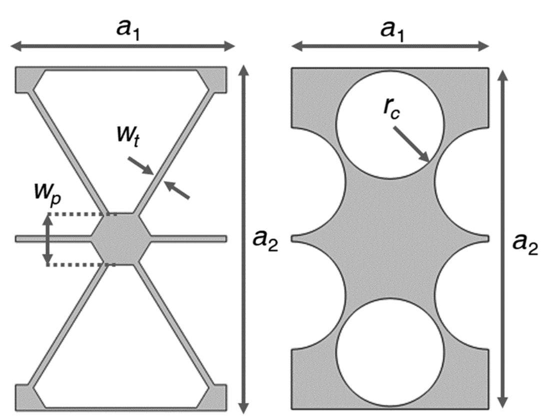

Device	a_1 (μm)	a_2(μm)	n_x	n_y	w$_p$(μm)	w$_t$(μm)	r_c(μm)
A [Fig. 1(a)]	100	172	12	7	30	2.5	–
B [Fig. 1(b)]	87	151	19	11	–	–	23
C	111	192	9	5	–	–	31
D	67	116	15	9	–	–	18
E	100	172	12	7	30	2.5	–

FIG. 2. The critical dimensions for the unit cells of all fabricated devices. The dimensions in the table are depicted above. n_x and n_y are the unit cell numbers of the PnC along the X and Y axes. The table entries are omitted where they do not apply. The fabricated devices for A and C include fillets of radii 2.5 μm at the sharp corners of the pad.

We present analyses of both finite and infinite PnC structures. A complete description of finite structures involves solving the 1D Euler-Bernoulli equation for the out-of-plane displacement $u(x,t)$, which describes the bending of the PnC beam. Such an analysis captures the behavior of the mode shape near the clamping points of the finite structure [30]:

$$\frac{d^2}{dx^2}\left[I(x)E\frac{d^2u(x)}{dx^2}\right] - \mathcal{T}\frac{d^2u(x)}{dx^2} - \rho_{1D}\frac{d^2u(x)}{dt^2} = 0, \tag{3}$$

where $I(x)$ is the geometric moment of inertia, E is the Young's modulus, $\mathcal{T}$ is the tension, and ρ_{1D} is the linear mass density. It can be seen that, for high-aspect-ratio devices, the fourth-order term is negligible away from the clamps [30].

For infinite structures, we can assume periodic boundary conditions. Thus, any expected mode shape should have a minimal contribution from the bending term in the Euler-Bernoulli equation. Under these conditions, the Euler-Bernoulli equation reduces to the 1D wave equation and thus the motion of the string is completely parametrized by its spatially dependent wave velocity:

$$v_{p,t} = \sqrt{\frac{\mathcal{T}}{\rho h \tilde{w}_{p,t}}}, \tag{4}$$

where ρ is the bulk density of the membrane, h is the membrane thickness, and $\tilde{w}_p$ ($\tilde{w}_t$) is the width of the converted pad (tether). Definitions of the converted pad and tether widths appear in Appendix A.

We outline the solution for infinite structures in Appendix B. As is typical in these types of problems, the band structure is parametrized by a transcendental equation:

$$\arccos S = ak, \tag{5}$$

$$S = \frac{(V+1)^2}{4V}\cos\left[\omega(t_p + t_t)\right] - \frac{(V-1)^2}{4V}\cos\left[\omega(t_p - t_t)\right], \tag{6}$$

where $t_{p,t} = l_{p,t}/v_{p,t}$ are the transit times of acoustic waves through the pad and tether, respectively, a is the unit cell length, k is the Bloch wave number, and $V \equiv v_t/v_p$ is what we define as the contrast. As can be seen in Eq. 4, the contrast V is geometrically defined by the mass contrast or the relative converted width of the pads and tethers. Traveling-wave solutions are prohibited when $|S| > 1$; such a condition defines the range of ω that determines all band gaps.

One goal of PnC design is to maximize the band-gap size in the frequency spectrum. For simplicity, we investigate the case in which we wish to maximize the width of the first band gap. Inspection of Eq. (6) reveals that this occurs when the second term is identically 0. In this case, $t_p = t_t$ and $|S|$ reaches its maximal value $S_{\max}$ when $\omega = \omega_\pi \equiv \pi/2t_t$:

$$S_{\max} = \frac{(V + V^{-1} + 2)}{4}. \tag{7}$$

With this in mind, we can derive an expression for the normalized band-gap width:

$$\Delta = \frac{\Delta\omega}{\omega_\pi} = \frac{2}{\pi} \arccos\left(-\frac{1 - 6V + V^2}{1 + 2V + V^2}\right). \tag{8}$$

Strong agreement between the 1D model prediction of Eq. (8) (blue line) and the FEM simulations of an equivalent 2D unit cell (points) across a range of contrasts can be seen in Fig. 3. The main source of error in the 2D-to-1D conversion arises from the inability of the 1D model to correctly account for the transition between the low-mass tethers and high-mass pads of the 2D PnC. In the high-mass-ratio limit, these regions account for a smaller fraction of the geometry and thus the 1D model better captures the resulting band structure for large V. Figure 3 also displays results for fabricated devices. It is readily seen that

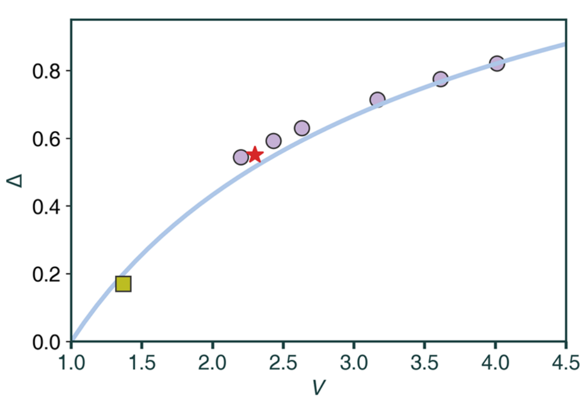

FIG. 3. The band-gap widths as a function of the mass contrast as determined from the 1D model: a comparison between different models of the band-gap to mid-gap ratio (Δ) versus the PnC contrast (V). The analytic prediction of the 1D model [Eq. (8)] (solid blue line), the FEM simulations of equivalent 2D structures (blue circle markers), and the experimental results of device A (red star marker) and device B (yellow square).

the device illustrated in Fig. 1(a) (red star) has a higher mass contrast compared to the device in Fig. 1(b) (yellow square). This difference in mass contrast is also reflected in the corresponding band-gap widths of both devices.

A technical point arises in the fabrication of devices in the limit of a very large band gap. As said before, V is determined by the relative sizes of the pads and tethers, with wide pads and narrow tethers giving rise to large values of V. Therefore, the minimum tether width that can be fabricated and the desired band-gap position set practical limits on V. As an example, a PnC with $V = 4$ would have pad widths of 40 μm assuming a $w_t = 1$ μm. The principle of equal transit times then sets the unit cell length to be 220 μm, which in turn sets $\omega_\pi = 2\pi \times 1$ MHz. In general, higher-contrast (higher-V) phononic crystals will have lower band-gap center frequencies, because the larger mass ratio induces lower average wave velocities.

B. Effects of contrast on soft clamping

The main advantages afforded by SiN PnCs include both soft clamping and phononic isolation of defect modes. We assert that V (and thus also Δ) is a geometrically defined indicator of the extent to which a PnC achieves these phenomena. To understand the effects of soft clamping on dissipation, we first examine the origin of bending loss for a given mechanical mode [11,12,17,31]:

$$Q_{\text{bend}} = Q_{\text{int}}(h)\frac{24(1-\nu^2)}{Eh^3}L_s(h)^{-1} = \frac{24(1-\nu^2)}{E_2(h)h^3}L_s(h)^{-1}, \tag{9}$$

$$L_s = \int \kappa(x,y)\, dx\, dy, \tag{10}$$

$$\kappa = \frac{1}{U}(\partial_x^2 u(x,y) + \partial_y^2 u(x,y))^2, \tag{11}$$

where $Q_{\text{int}}(h)$ is the intrinsic Q of silicon nitride, E is the Young's modulus, h is the nitride thickness, ν is the Poisson ratio, U is the kinetic energy of the mode, and $u(x,y)$ is the mode shape. $E_2(h)$ is the effective imaginary part of the Young's modulus, defined to be $E_2 = E/Q_{\text{int}}$. Here, we call attention to the dependence of Q_{int}, which has been shown to have a scaling $Q_{\text{int}} \propto h$ at membrane thicknesses around and below 100 nm where surface loss dominates [32]. We will call $L_s(h)$ the loss factor, which quantifies the bending losses associated with a given mode. From Eq. (11), one can see that $L_s(h) \propto h^{-1}$. Therefore, we expect $Q \propto h^{-1}$ for soft-clamped PnCs [17]. We also define κ as the loss density, which describes the spatial distribution of lossy motion of a mode. Therefore, the bending loss in membrane devices is most pronounced at clamping points, where the mode shape curves strongly to adhere to the restrictive clamping boundary conditions.

Soft clamping and phononic isolation occur when the mechanical defect mode has a frequency within the acoustic band gap of the PnC. Within the band gap, k becomes complex. The magnitude of $\mathrm{Im}(k)$ at the defect-mode frequency determines the decay length $l_0 = 1/\mathrm{Im}(k)$ of the defect mode into the PnC.

To directly illustrate how PnC design affects the soft clamping of defect modes, we perform a series of 1D simulations where a single defect is placed in a series of PnCs with ascending contrast. From the calculated defect-mode shapes, one can predict a value for Q_{bend}, assuming that Q_{int} has a value of 6600 [32]. In this 1D simulation, the defect mode's frequency has a nearly constant position relative to the band-gap center [Fig. 4(a)]. Two effects as a function of increasing Δ are apparent. First, the normalized mechanical decay length $n_0 = l_0/a$ decreases as a function of Δ [Fig. 4(b)], as predicted from our analytic analysis in the 1D model. Second, a decrease of Q_{bend} is apparent. This is indicative of the bending resulting from the strong decay into the PnC.

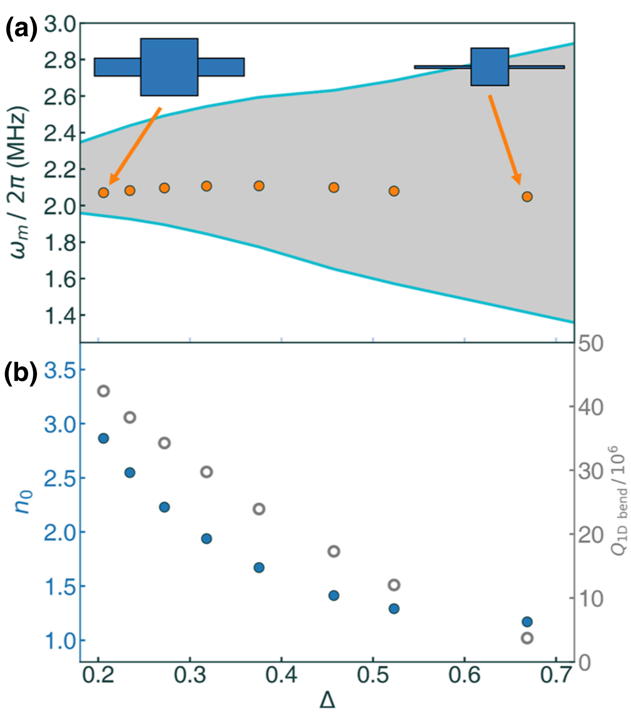

FIG. 4. The effects of contrast for 1D PnCs with a constant defect geometry. (a) The orange points are the fundamental defect-mode frequencies across all simulated structures. The shaded region denotes the frequency range of the simulated band gaps. The insets in (a) are schematics of the simulated 1D unit cell at the lower extreme (left) and upper extreme (right) of the band-gap width. (b) The normalized-mode amplitude-decay length (blue) and quality factors (gray) for 1D PnC strings with a constant defect. We define $n_0 = l_0/a$, where l_0 is the exponential decay length. At large contrasts, n_0 approaches 1 because the defect mode does not begin to decay until the onset of the PnC.

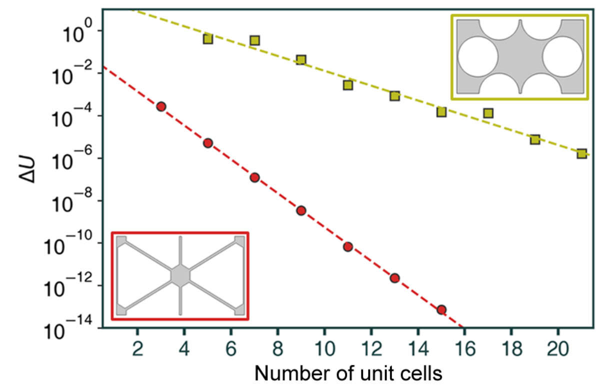

FIG. 5. The kinetic energy in the PnC frame, normalized to the total energy, in both high-contrast (red points, $V = 2.3$) and low-contrast (yellow points, $V = 1.3$) PnCs as calculated from FEM simulations. The insets are the unit cells used in the simulation. The dashed lines are fits assuming exponential energy decay for the defect mode. The decay length for the high-contrast unit cell (red fit) is 0.54 unit cells. The decay length from the low-contrast unit cell (yellow fit) is 1.24 unit cells.

C. Effect of contrast on phononic isolation

The numerical analysis above shows that high-contrast PnCs exhibit short defect-mode decay lengths and we also see numerically that this short decay length provides enhanced suppression of radiative loss. In this analysis, we investigate the concept of phononic isolation in a 2D structure by FEM simulation using COMSOL (for details, see Appendix D). Here, we calculate the ratio of the tensile energy stored in the entire structure to the energy stored in a 10-μm overhang around the PnC perimeter. We define this ratio as ΔU. As seen in Fig. 5, the higher-contrast PnC has a faster energy decay compared to the low-contrast crystal. We note that in the 1D case, S_{max} is reached when the defect-mode frequency is at the center of the band gap. However, even if this condition is not obtained, one can still achieve robust isolation in the high-contrast limit.

D. Beyond the 1D model: Incorporating defects in 2D

Up to this point, we have focused on PnC characteristics and have shown that our 1D model reproduces the basic behavior of the equivalent 2D crystals. However, the same cannot be done for designing defects in two dimensions, where we generally find that the 1D results have at most a qualitative relationship to a 2D defect. This is mostly due to the complicated stress redistribution that occurs in intricate 2D structures around the defect (Fig. 7), which a 1D model cannot fully capture. This internal structure of the defect leads us to further divide the loss pathways in our 2D devices into losses that can encapsulated in 1D simulations ($Q_{\mathrm{1D-bend}}$) and losses that are inherently 2D ($Q_{\mathrm{2D-bend}}$). In this next section, for example, we design five different devices with various combinations of defects and

PnC designs (Fig. 7). FEM simulations of the defect-mode shape help illustrate the difference between the aforementioned separation between "1D loss" and "2D loss." For example, in the context of high-contrast PnCs, a line cut of the defect mode of device A closely resembles a string mode emanating radially from the PnC center. Device E has a large defect pad, and therefore there is considerable internal motion of the pad. This internal motion gives rise to a larger participation ratio of the "2D loss" as compared to device A. Therefore, one expects that 1D analysis is much more applicable to device A than to device E.

The stress redistribution of the 2D structure also strongly affects the position of the defect-mode frequency within the band gap, leading to discrepancies between the 1D and 2D simulations. While the 1D model allows positioning of the defect modes directly in the band-gap center [Fig. 4(a)], the equivalent mode has a lower frequency in both the 2D FEM simulations and the experimental results [Fig. 1(e)].

III. EXPERIMENTAL RESULTS

To test examples of the above ideas, we fabricate and characterize multiple devices (Fig. 7), utilizing the two different PnC designs illustrated in Fig. 1 and defined in Fig. 2, and multiple defect designs. The chosen devices illustrate the complex interplay of bending loss (both in the PnC and defect) and effective mass m (characterized by x_{zp}) of the defect mode. The phononic devices are patterned into a 100-nm-thick low-pressure chemical-vapor deposition (LPCVD) silicon-nitride layer on a silicon substrate and suspended using a KOH wet etch. All of the Si substrates are 375 μm thick 5×5 mm^2 in the transverse dimensions. Full fabrication information appears in Appendix C.

The mechanical mode spectrum of the devices is characterized at both room temperature and 4 K by affixing the device to a stack consisting of a mirror mounted on a piezoelectric transducer, all mounted on the sample stage (the cold stage for the 4-K measurements) as illustrated in Fig. 6. The spectrum is imprinted on the amplitude fluctuations of light reflected from the etalon formed by the mirror and the membrane device. For all measurements, around 5 mW of 1064 nm laser power is incident on the sample. Classical heating calculations indicate that this amount of laser power should induce less than 1 K of heating. This is consistent with other works where high-aspect-ratio silicon-nitride devices thermalize to cryogenic conditions in high-finesse optical cavities [27,33]. An absolute calibration of the mechanical displacement of our devices can be performed by assuming that the observed mechanical amplitude is entirely due to the expected thermal signal. However, many of our spectra are taken via white-noise driving of the entire PnC chip via the piezoelectric transducer. Therefore, all mechanical amplitudes are displayed relative to the

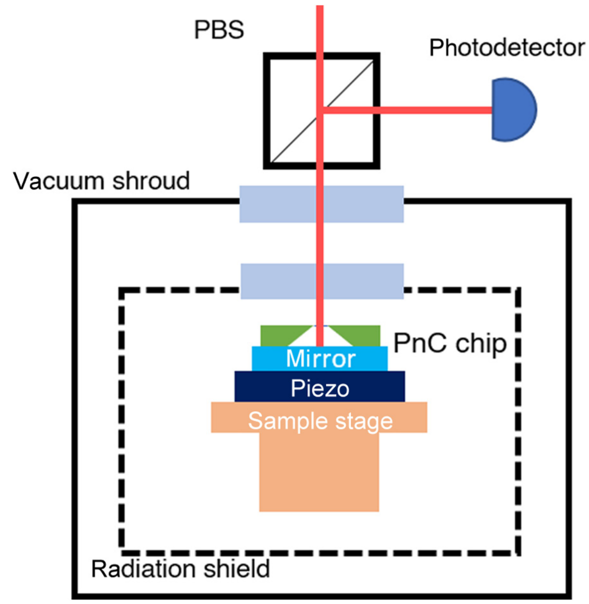

FIG. 6. A schematic of the experimental apparatus used for measuring both the mechanical spectra and the ringdowns. The mechanics chip (green) is affixed atop a stack consisting of a piezoelectric transducer ("piezo," dark blue) and a highly reflective mirror (light blue). This stack is mounted onto a stage linked to the sample stage (cold stage) for room-temperature (4-K) measurements. The solid box represents the vacuum shroud for both the room-temperature and the 4-K apparatus, while the dashed box represents the radiation shield present for 4-K measurements. The light reflected off the stack is sent to a photodiode via a polarizing beam splitter.

shot-noise-limited noise floor the detection chain. The room-temperature measurements are performed at a pressure less than 10^{-6} mBar. The 4-K measurements are performed in a closed-cycle cryostat with free-space optical access.

To clearly understand the mode spectrum, we characterize the motion in multiple regions of the PnC. As outlined in Fig. 1, the different-colored spectra are obtained by probing near the defect (orange point) and in the crystal bulk (blue point). Modes that only appear when probing near the defect are confined by the PnC and considered to be defect modes [Figs. 1(e) and 1(f)]. When probing in the crystal bulk [Figs. 1(c) and 1(e)], one sees a wide range of frequencies with no discernible mechanical resonance [the gray regions in Figs. 1(c)–1(f)]. This frequency range is found to be broader for the high-contrast PnC depicted in Fig. 1(a) and is in accordance with the results of the FEM simulations. We note that in order to adequately resolve the upper band-gap edge, we choose to measure on a tether, as it accommodates more high-frequency motion above the band gap than in the pads of the PnC. Occasionally, spurious modes are found inside the band gap (Fig. 1). These modes have quality factors on the order

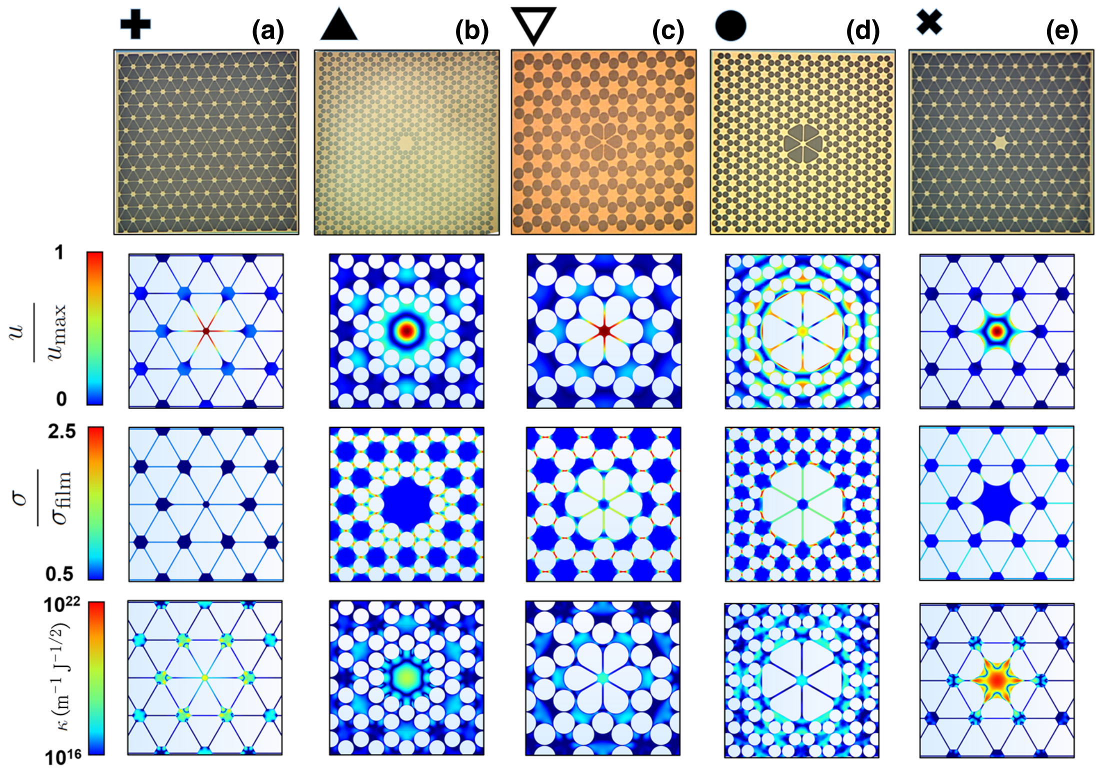

FIG. 7. A compilation of all the devices presented in this work. In the first row are optical-microscope images of suspended phononic structures. Above are device labels that correspond to device properties plotted in Fig. 8. The second row presents FEM simulations of symmetric defect-mode shapes. The third row shows FEM simulations of the static stress distribution normalized to the film stress. The fourth row displays the normalized bending loss density.

of 100 and therefore are inconsistent with pure-silicon-nitride membrane modes. This is consistent with the fact that these are hybridized modes between the membrane and its substrate or the chip-mirror assembly [20].

Quality factors are determined via ringdown measurements of the phononic structures driven by the piezoelectric transducer. Quality-factor measurements are performed in the linear regime. The drive is swept across the mechanical resonance to verify a Lorentzian line shape and if a nonsymmetric Duffing line shape is observed, the drive power is dropped by 10 dB until the linear regime is reached. Figure 8(a) displays the quality factors for the symmetric modes of all devices at both room temperature and 4 K. The loss factors are calculated using Eq. (9) via FEM simulations of each device. The fits are based on the assumption that the dissipation is bending-loss limited: $Q_{\text{rad}} \ll Q_{\text{bend}}$. For the room-temperature data, the fitted value of $E_2 = 80$ MPa combined with the assumption of $E = 250$ GPa infers that $Q_{\text{int}} = 3125$. This is in agreement with tabulated values of Q_{int} found in the literature [32]. The fitted value of $E_2 = 17$ MPa at 4 K infers that $Q_{\text{int}} = 14\,700$. We note that the scatter of points, particularly at room temperature, indicates that this assumption may not hold for all devices. Notably, device C has a rather large value of ΔU, which may be indicative of the existence of a measurable external loss for this device.

In Fig. 8(b), we see the force-sensing performance across all devices at both room temperature and 4 K. As discussed previously, we use force-sensing performance of these high-frequency resonators as a comparison metric. First, let us comparatively examine devices A and B. Device A displays among the best performance among all devices, with a force sensitivity of 12 aN/$\sqrt{\text{Hz}}$ at 1.6 MHz at 4 K. Both devices A and B contain a well-confined defect mode, leading to a relatively large $x_{\text{zp}} >$ 1 fm at megahertz frequencies. This confinement is accomplished simultaneously with little dissipation. For device A (Fig. 7), the bending loss of the fundamental trampoline mode is most pronounced in the pads surrounding the defect itself. This type of bending profile is similar to that seen in SiN trampolines [14,15], while relaxing some of the clamping effects at the edge of the defect mode. Device B maintains low dissipation via the soft clamping of its surrounding low-contrast PnC. Although both devices demonstrate relatively high force sensitivity, they differ considerably in design and therefore include clear design tradeoffs. Device A has low effective mass due to its low physical mass. Additionally, the low effective mass of device A can also be attributed to its first-order symmetric

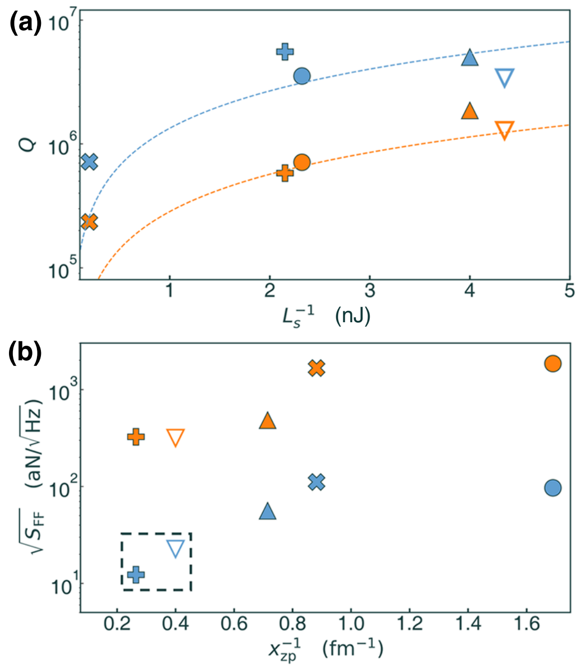

FIG. 8. (a) The dependence of the quality factor on the loss factor L_s for all fabricated devices, measured at room temperature (orange) and at 4 K (blue). The symbols correspond to the key presented in Fig. 7. The dashed lines represent calculated Q values from Eq. (9), with $E_2 = 80$ MPa for the room-temperature data and $E_2 = 17$ MPa for 4 K. (b) The calculated force sensitivity at room temperature (orange) and at cryogenic conditions (blue). The box is to emphasize the similarity in defect design and performance between devices A and C.

mode, which is generally lower in mass since it has a node of motion at the defect boundary. However, its frequency is close to the band-gap edge (Fig. 1). This frequency is most strongly influenced by the length of the defect tethers [14] and thus the frequency cannot easily be pushed higher. Device B has a second-order symmetric defect mode. In general, these second-order modes are easier to place in the band-gap center but are at higher mass because the edge of the defect coincides with an antinode of motion.

To compare the effects of the PnC on the defect mode, we can compare devices A and C, both of which have defects with trampoline geometries. Both devices also support a first asymmetric defect mode with frequencies between 1.5 and 2 MHz. We find overall that these devices exhibit a similar force sensitivity both experimentally [Fig. 8(b)] and in the FEM simulations. There are, however, slight differences in how these devices achieve their sensitivity. The FEM simulations predict that device C will have more soft clamping and hence a higher Q value than device A (although in experiment device A has a higher Q value, perhaps due to its larger number of unit cells). However, device A has lower mass and hence larger x_{zp} than device C. Note that even when the defect pad width of device C is set to be identical to that of device A, the increase in pad width is associated with an increase in resonant frequency and the same conclusions hold.

The remaining devices (D and E) provide examples of how nuances in device design can cause adverse effects. For instance, device D exhibits a relatively low x_{zp} [Fig. 8(b)]. Here, the defect accommodates the second symmetric mode, causing the PnC to carry a large portion of the defect motion (Fig. 7). This differs from the fundamental trampoline mode shape in that the second symmetric mode has an antinode of motion at the PnC boundary. Thus the motion of the defect strongly drives the motion of the surrounding low-contrast crystal, adding considerable mass to the mode. This effect is not seen in device C (same PnC, different defect), because this defect is designed to accommodate the fundamental mode within the band gap. Finally, device E is composed of a large defect pad intended to isolate the second symmetric mode through the PnC. which leads to a large amount of defect loss. The large pad is largely stress released and thus the edges of the pad are allowed to bend freely (Fig. 7). We can compare this to device A, which has a large released pad, but it is surrounded by a highly stressed boundary. The relieved stress regions accommodate extreme bending, which leads to substantial internal loss, thus limiting the Q. This effect has ramifications for future PnC design, where a large pad is often desired for efficient coupling between an optical mode and the mechanical motion.

IV. CONCLUSION

To summarize, we study SiN membrane designs composed of a defect surrounded by a PnC structure. We demonstrate the effects that high-contrast PnCs can have on producing wide band gaps. Additionally, we present numerical analysis that connects high-contrast PnCs to robust energy isolation of defect modes. Conversely, high-contrast crystals compress the mode spatial distribution, induce more bending, and increase the internal loss. However, the increased internal loss is not severe for certain designs and may, for some applications, be worth the tradeoff for phononic isolation and requirements on the number of unit cells. We show that a 1D model with proper conversion, based on the Euler-Bernoulli equation or its reduction to the wave equation, is suitable for analyzing the behavior of a 2D PnC structure. However, incorporation of a defect into a 2D crystal requires a complex redistribution of the stress, which can only be achieved by a suitable FEM simulation.

Utilizing these tools, we design, fabricate, and measure five devices differing in PnC contrast and defect designs. These devices exhibit force sensitivity on the order 10 aN/$\sqrt{\text{Hz}}$ at 4 K. We draw attention to both devices A and C, which we predict to have comparable force sensitivities when bending-loss limited. This similar performance is achieved despite the vast difference between the PnCs of the devices and we attribute this similarity in force sensitivity to the low-mass trampoline defect common to both devices. However, under conditions in which both of these devices are radiation-loss dominated, device A has the potential to outperform device C in force sensitivity due to its robust acoustic isolation or, equivalently, achieve equal radiation isolation with a smaller number of unit cells.

For force-sensing functionalization, it is generally required to add additional components to the device to induce a force between the resonator and to detect the subsequent displacement in a separate location. Device B has the advantage that it has the largest area on which to deposit samples and probe the motion, in comparison to the smaller defects that lead to the highest force sensitivity in devices A and C. However, the placement of samples on the high-stress tethers of the low-mass trampoline defect archetypes of devices A and C produces minimal effects on the dissipative properties, as demonstrated in Ref. [25]. Further, any additional elements add mass and alter the designed mechanical mode shapes and properties. Hence, an additional consideration is to position and maintain the defect within the band gap. The wide band gaps of high-contrast PnCs can tolerate larger changes in defect mass. However, low-mass defects such as the one in device A display a first symmetric mode at the lower end of the band gap. Therefore, in practice, this device would be limited to small sample masses, to avoid pushing the mechanical frequency below the lower band edge. The challenge of positioning the defect mode within the band gap can be averted by exploring more exotic defects beyond the trampoline archetype, such as delocalized double-pad defects, or by utilizing higher-order modes.

As mentioned earlier, the low-frequency modes or, notably, the fundamental mode frequencies (ω_0 in Table I) of a mechanical structure can induce instabilities when placed inside an optical cavity due to their Brownian motion. High-contrast PnCs (devices A and E) can achieve mode localization and acoustic isolation with fewer unit cells (Fig. 2), potentially reducing the total device size. While smaller devices have higher fundamental mode frequencies, the fundamental modes of high-contrast devices have low effective masses when compared to their low-contrast counterparts and thus have more Brownian motion. Ultimately, the effect on the cavity stability will be determined by the complete mechanical spectrum and the most relevant effects will be dependent on the optical cavity in question.

All devices reported in this work are fabricated with a thickness of 100 nm. However, by using a thickness of 20 nm SiN or less, the force sensitivity could be significantly enhanced due to the scaling of $\sqrt{S_{\mathrm{FF}}} \propto h$ for soft-clamped membranes. Reduction of the thickness of device A to 20 nm would optimally improve its force sensitivity to 2 aN/$\sqrt{\mathrm{Hz}}$ at 4 K.

Lastly, a large influence on device design is the operating temperature of the experiment. Where the bending loss is high, such as at room temperature, strongly soft-clamped devices with low-contrast PnCs, such as devices B and C, should be employed. At temperatures around or below 100 mK, the E_2 of silicon nitride dramatically decreases, greatly diminishing the bending-loss contribution to the total dissipation of a mechanical mode [13]. In this regime, radiative losses have the potential to be the dominating loss pathways [34]; thus devices based around high-contrast high-isolation PnCs (devices A and E) may become more attractive, as they offer lower dissipation with lower mass defects. With this in mind, a consideration for future studies will be the effect of the tether size on thermalization of different PnC designs to the cryogenic environment.

ACKNOWLEDGMENTS

We acknowledge funding from the U.S. Air Force Office of Scientific Research (AFOSR) Presidential Early Career Award in Science and Engineering (PECASE), the National Science Foundation (NSF) under Grant No. PHYS 1734006, the U.S. Army Research Office (ARO)–Laboratory for Physical Sciences (LPS) Cross-Quantum Systems Science & Technology program (Grant No. W911NF-18-1-0103), and a Cottrell Scholar award. We thank Yeghishe Tsaturyan for helpful discussions.

APPENDIX A

We present here the method for converting a 2D unit cell geometry to an effective 1D geometry. This approach

TABLE I. A tabulation of the key parameters for each symmetric defect mode for all of the fabricated devices. Note the correlation between Δ and phononic isolation (ΔU).

Device	$\omega_m/2\pi$ (MHz)	x_{zp} (fm)	Δ	ΔU	w_{defect} (μm)	$\omega_0/2\pi$ (kHz)
A	1.65	3.8	0.55	5.6×10^{-7}	15	189
B	2.55	1.4	0.17	2.3×10^{-2}	130	174
C	1.70	2.2	0.19	6.9×10^{-2}	30	242
D	3.41	0.6	0.24	3.2×10^{-2}	30	246
E	2.39	1.1	0.55	1.9×10^{-8}	80	181

involves first considering a wave direction $\hat{k}$ along which we will convert the 2D geometry. We wish to encode the geometry transverse to the wave direction into the resulting 1D geometry. It is known that 1D strings with variable width will have lower wave velocities in the wider regions. We imagine that with more transverse mass, the plane wave in the 2D geometry will also have a lower wave velocity. Our conversion will then be as follows:

$$g_{1D}(x_l) = \int_G g(x_l, x_t) dx_t, \tag{A1}$$

where x_l and x_t refer to the coordinates along the longitudinal and transverse wave directions, respectively, and G refers to the domain of a single unit cell.

Upon performing the conversion, $g_{1D}(x)$ gives a continuous variable width of the beam from which a variable wave velocity can be derived. To derive the band structure, the 1D wave equation with Floquet boundary conditions can be numerically solved for an arbitrary $g_{1D}(x)$. However, we find it fruitful to further simplify the geometry where possible. Namely, we wish to convert the wave velocity to match that of the Kronig-Penney model, which can be solved analytically. This involves defining regions of high mass and low velocity (pads) and low mass and high velocity (tethers) from an arbitrary $g_{1D}(x)$.

For unit cells such as those in device A, the selection of the pad and tether regions follows naturally from the 2D geometry. Furthermore, the integration carried out in Eq. (A1) can be done using geometric properties. This procedure will perform the transformation $(w_p, w_t, l_p, l_t) \rightarrow (\tilde{w}_p, \tilde{w}_t, \tilde{l}_p, \tilde{l}_t)$ of the geometric parameters. This process is illustrated in Fig. 9.

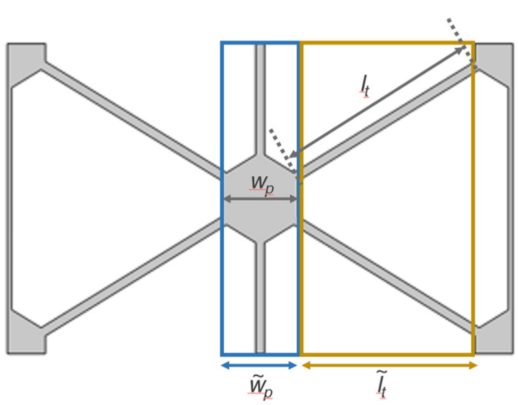

FIG. 9. The geometry of the 2D-to-1D conversion for a pad-tether unit cell. The blue box (orange box) defines the pad region (tether region) of the PnC unit cell.

Following this procedure, we derive the following:

$$\rho_p = \frac{\sqrt{3}}{2} w_p h \rho + \frac{l_t t_w h}{w_p}, \tag{A2}$$

$$\rho_t = \frac{4}{\sqrt{3}} w_p h \rho, \tag{A3}$$

$$\tilde{l}_p = l_p, \tag{A4}$$

$$\tilde{l}_t = \frac{\sqrt{3}}{2} l_t, \tag{A5}$$

$$\tilde{\mathcal{T}} = \frac{4}{\sqrt{3}} \sigma t_w h, \tag{A6}$$

$$\tilde{v}_p = \left[\frac{3 w_p \rho}{8 t_w \sigma} + \frac{\sqrt{3} l \rho}{4 w_p \sigma} \right]^{-1/2}, \tag{A7}$$

$$\tilde{v}_t = \sqrt{\frac{\sigma}{\rho}}. \tag{A8}$$

In this work, we also study unit cells that do not fit the pad-tether model at the outset [17]. Figure 10 shows an example collapse in relation to the 2D unit cell. $g_{1D}(x)$ exhibits pronounced dips over short regions, which we will

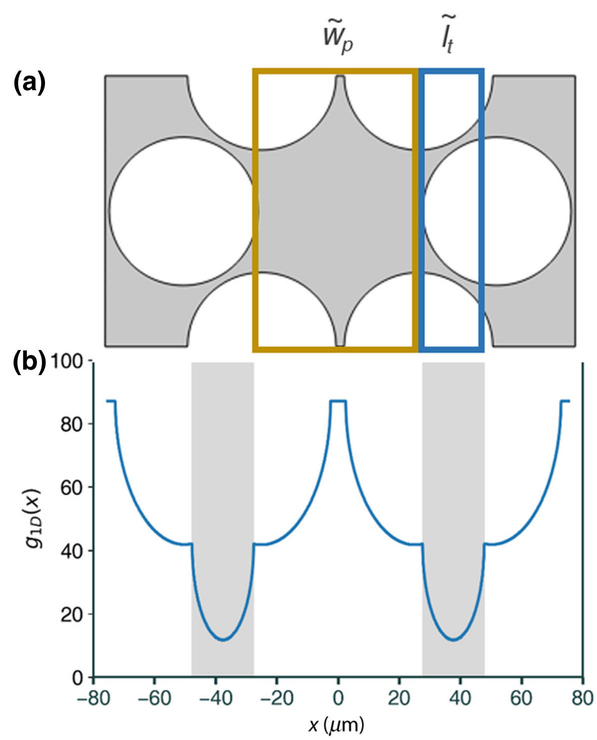

FIG. 10. A schematic of 1D collapse for a low-contrast unit cell. (a) The definition of the pad and tether regions inside the low-contrast unit cell. (b) The 1D geometry that results from performing the collapse: the gray regions indicate the high-velocity tether regions used to define V for this unit cell.

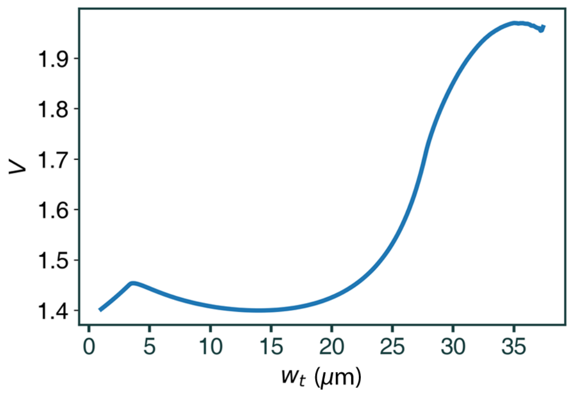

FIG. 11. The distribution of contrast values derived from different partitioning of the 1D geometry.

call the tether regions; all other regions will be considered pads. We can then extract the pad width and tether width by taking the mean width over both regions. It is of note that the definition of the pad and tether regions is an arbitrary choice. However, we see that over a reasonable and wide range of tether definitions, V stays roughly constant between 1.4 and 1.5 (Fig. 11).

APPENDIX B

In this appendix, we present a detailed derivation of the band structure in the 1D model. We assume that the displacement field has the following form:

$$y_k = A_k e^{ikx-i\omega t} + B_k e^{-ik-i\omega t}. \tag{B1}$$

In this model, we view the PnC structure as a modulation of the acoustic wave expressed in Eq. (B1). Interfaces between pads and tethers will then have reflection and transmission coefficients given as the following familiar Fresnel coefficients:

$$r_{pt} = \frac{v_t - v_p}{v_t + v_p}, \tag{B2}$$

$$t_{pt} = \frac{2v_t}{v_t + v_p}, \tag{B3}$$

$$r_{tp} = \frac{v_p - v_t}{v_t + v_p}, \tag{B4}$$

$$t_{tp} = \frac{2v_p}{v_t + v_p}. \tag{B5}$$

To continue with our analysis, we can derive the motion across as a unit cell as a transfer matrix M, which describes the transformation of the amplitude coefficients A_k and B_k across each unit cell of the PnC. The total matrix M will then just be a product of the matrices for each subsection:

$$M = M_{hp} M_{tp} M_t M_{pt} M_{hp}. \tag{B6}$$

Here, M_{hp} captures the accumulated phase of the plane waves across the half pads at either end of the unit cell. M_t does the same for the tether section, while M_{tp} and M_{pt} account for transmission and reflection at each interface:

$$M_{hp} = \begin{pmatrix} e^{ik_p l_p/2} & 0 \\ 0 & e^{-ik_p l_p/2} \end{pmatrix}, \tag{B7}$$

$$M_{pt} = \begin{pmatrix} t_{pt} - \dfrac{r_{tp} r_{pt}}{t_{tp}} & \dfrac{r_{tp}}{t_{tp}} \\ -\dfrac{r_{pt}}{t_{tp}} & \dfrac{1}{t_{tp}} \end{pmatrix}, \tag{B8}$$

$$M_t = \begin{pmatrix} e^{ik_t l_t} & 0 \\ 0 & e^{-ik_t l_t} \end{pmatrix}, \tag{B9}$$

$$M_{tp} = \begin{pmatrix} t_{tp} - \dfrac{r_{pt} r_{tp}}{t_{pt}} & \dfrac{r_{pt}}{t_{pt}} \\ -\dfrac{r_{tp}}{t_{pt}} & \dfrac{1}{t_{pt}} \end{pmatrix}. \tag{B10}$$

If we assume that our structure is infinite, then the Bloch condition implies

$$\begin{pmatrix} A_1 \\ B_1 \end{pmatrix} = e^{iKa} \begin{pmatrix} A_0 \\ B_0 \end{pmatrix}, \tag{B11}$$

where

$$\begin{pmatrix} A_1 \\ B_1 \end{pmatrix} = M \begin{pmatrix} A_0 \\ B_0 \end{pmatrix}. \tag{B12}$$

Therefore, we have the following eigenvalue problem:

$$\begin{pmatrix} M_{11} & M_{12} \\ M_{21} & M_{22} \end{pmatrix} \begin{pmatrix} A_0 \\ B_0 \end{pmatrix} = e^{iKa} \begin{pmatrix} A_0 \\ B_0 \end{pmatrix}. \tag{B13}$$

We note that M is a product of unitary matrices, which places a constraint on its components:

$$M_{11} M_{22} - M_{12} M_{21} = 1. \tag{B14}$$

Solving the eigenvalue problem gives us the implicit bandgap equations:

$$e^{iKa} = S \pm \sqrt{S^2 - 1}, \tag{B15}$$

$$S \equiv \frac{M_{11} + M_{22}}{2}, \tag{B16}$$

or, written more explicitly,

$$S = \frac{(V+1)^2}{4V} \cos\omega(t_p + t_t) - \frac{(V-1)^2}{4V} \cos\omega(t_p - t_t). \tag{B17}$$

APPENDIX C

The devices are fabricated on a 375-μm-thick 3-in. diameter silicon wafer, with 100 nm of grown stoichiometric LPCVD silicon nitride on either side. The designs are patterned using a direct-write photolithography system after spinning 1 μm of SPR-660 photoresist onto either side. The top of the wafer is patterned with the PnC designs, while the back is patterned with rectangular windows aligned to each PnC. The patterning is done on both sides with $300\,\mathrm{mJ\,cm^{-2}}$ of 405-nm light. During these steps, the wafer is affixed to a sapphire carrier wafer with Crystalbond 509, in order to protect the bottom side from unwanted processing. Patterning of the silicon nitride is completed via a CF_4 reactive ion etch. The wafer is then cleaned with O_2 plasma, followed by ultrasound cleaning in an acetone bath. Additional cleaning is performed with isopropyl alcohol and water. To suspend the PnC structures, the window side of the wafer is etched using an 80-C KOH bath. The PnC side is protected via a PEEK wafer holder. Following wet etching, the wafer is cleaned in a Nanostrip bath, acetone, and isopropyl alcohol.

APPENDIX D

The FEM simulations in this work are performed using COMSOL Multiphysics. The simulations are performed in two steps; the stationary stress redistribution is calculated, followed by an eigenfrequency analysis to determine the mode spectrum of each PnC. The simulations are performed with increasingly fine meshes until both the mode frequencies and the loss factors are found to converge to a change of less than 5%. These simulations assume that the density of silicon nitride is $3100\,\mathrm{kg\,m^{-3}}$, the film stress is 1.13 GPa, the Poisson ratio is 0.27, and the Young's modulus is 250 GPa.

[1] D. Rugar, R. Budakian, H. Mamin, and B. Chui, Single spin detection by magnetic resonance force microscopy, Nature **430**, 329 (2004).

[2] M. Poggio and C. Degen, Force-detected nuclear magnetic resonance: Recent advances and future challenges, Nanotechnology **21**, 342001 (2010).

[3] A. H. Safavi-Naeini and O. Painter, Proposal for an optomechanical traveling wave phonon-photon translator, New J. Phys. **13**, 32 (2010).

[4] A. Higginbotham, P. Burns, M. Urmey, R. Peterson, N. Kampel, B. Brubaker, G. Smith, K. Lehnert, and C. Regal, Harnessing electro-optic correlations in an efficient mechanical converter, Nat. Phys. **14**, 1038 (2018).

[5] P. Rabl, S. J. Kolkowitz, F. H. L. Koppens, J. G. E. Harris, P. Zoller, and M. D. Lukin, A quantum spin transducer based on nanoelectromechanical resonator arrays, Nat. Phys. **6**, 602 (2010).

[6] M. Aspelmeyer, T. J. Kippenberg, and F. Marquardt, Cavity optomechanics, Rev. Mod. Phys. **86**, 1391 (2014).

[7] K. Ekinci and M. Roukes, Nanoelectromechanical systems, Rev. Sci. Instrum. **76**, 061101 (2005).

[8] I. Wilson-Rae, Intrinsic dissipation in nanomechanical resonators due to phonon tunneling, Phys. Rev. B. **77**, 245418 (2008).

[9] S. S. Verbridge, H. G. Craighead, and J. M. Parpia, A megahertz nanomechanical resonator with room temperature quality factor over a million, Appl. Phys. Lett. **92**, 13112 (2008).

[10] B. M. Zwickl, W. E. Shanks, A. M. Jayich, C. Yang, A. C. B. Jayich, J. D. Thompson, and J. G. E. Harris, High quality mechanical and optical properties of commercial silicon nitride membranes, Appl. Phys. Lett. **92**, 103125 (2008).

[11] Q. P. Unterreithmeier, T. Faust, and J. P. Kotthaus, Damping of Nanomechanical Resonators, Phys. Rev. Lett. **105**, 027205 (2010).

[12] P.-L. Yu, T. Purdy, and C. Regal, Control of Material Damping in High-Q Membrane Microresonators, Phys. Rev. Lett. **108**, 083603 (2012).

[13] M. Yuan, M. A. Cohen, and G. A. Steele, Silicon nitride membrane resonators at millikelvin temperatures with quality factors exceeding 10^8, Appl. Phys. Lett. **107**, 263501 (2015).

[14] R. A. Norte, J. P. Moura, and S. Gröblacher, Mechanical Resonators for Quantum Optomechanics Experiments at Room Temperature, Phys. Rev. Lett. **116**, 147202 (2016).

[15] C. Reinhardt, T. Müller, A. Bourassa, and J. C. Sankey, Ultralow-Noise SiN Trampoline Resonators for Sensing and Optomechanics, Phys. Rev. X **6**, 021001 (2016).

[16] A. Z. Barasheed, T. Müller, and J. C. Sankey, Optically defined mechanical geometry, Phys. Rev. A **93**, 053811 (2016).

[17] Y. Tsaturyan, A. Barg, E. S. Polzik, and A. Schliesser, Ultracoherent nanomechanical resonators via soft clamping and dissipation dilution, Nat. Nanotech. **12**, 776 (2017).

[18] A. H. Ghadimi, S. A. Fedorov, N. J. Engelsen, M. J. Bereyhi, R. Schilling, D. J. Wilson, and T. J. Kippenberg, Elastic strain engineering for ultralow mechanical dissipation, Science **360**, 764 (2018).

[19] T. P. M. Alegre, A. Safavi-Naeini, M. Winger, and O. Painter, Quasi-two-dimensional optomechanical crystals with a complete phononic bandgap, Opt. Express **19**, 5658 (2010).

[20] P.-L. Yu, K. Cicak, N. Kampel, Y. Tsaturyan, T. Purdy, R. Simmonds, and C. Regal, A phononic bandgap shield for high-Q membrane microresonators, Appl. Phys. Lett. **104**, 023510 (2014).

[21] Y. Tsaturyan, A. Barg, A. Simonsen, L. G. Villanueva, S. Schmid, A. Schliesser, and E. S. Polzik, Demonstration of suppressed phonon tunneling losses in phononic bandgap shielded membrane resonators for high-Q optomechanics, Opt. Express **22**, 6810 (2014).

[22] G. D. Cole *et al.*, Tensile-strained $In_xGa_{1-x}P$ membranes for cavity optomechanics, Appl. Phys. Lett. **104**, 201908 (2014).

[23] M. Bückle, V. C. Hauber, G. D. Cole, C. Gärtner, U. Zeimer, J. Grenzer, and E. M. Weig, Stress control of tensile-strained $In_{1-x}Ga_xP$ nanomechanical string resonators, Appl. Phys. Lett. **113**, 201903 (2018).

[24] N. Scozzaro, W. Ruchotzke, A. Belding, J. Cardellino, E. C. Blomberg, B. A. McCullian, V. P. Bhallamudi,

D. V. Pelekhov, and P. C. Hammel, Magnetic resonance force detection using a membrane resonator, J. Magn. Reson. **271**, 15 (2016).

[25] R. Fischer, D. P. McNally, C. Reetz, G. G. T. Assumpcao, T. R. Knief, Y. Lin, and C. A. Regal, Spin detection with a micromechanical trampoline: Towards magnetic resonance microscopy harnessing cavity optomechanics, New J. Phys. **21**, 043049 (2019).

[26] R. Andrews, R. Peterson, T. Purdy, K. Cicak, R. Simmonds, C. Regal, and K. Lehnert, Bidirectional and efficient conversion between microwave and optical light, Nat. Phys. **10**, 321 (2014).

[27] T. P. Purdy, R. W. Peterson, P.-L. Yu, and C. A. Regal, Cavity optomechanics with Si_3N_4 membranes at cryogenic temperatures, New J. Phys. **14**, 115021 (2012).

[28] J. M. Nichol, E. R. Hemesath, L. J. Lauhon, and R. Budakian, Nanomechanical detection of nuclear magnetic resonance using a silicon nanowire oscillator, Phys. Rev. B **85**, 054414 (2012).

[29] P. R. Saulson, Thermal noise in mechanical experiments, Phys. Rev. D. **42**, 2437 (1990).

[30] S. A. Fedorov, N. J. Engelsen, A. H. Ghadimi, M. J. Bereyhi, R. Schilling, D. J. Wilson, and T. J. Kippenberg, Generalized dissipation dilution in strained mechanical resonators, Phys. Rev. B **99**, 054107 (2019).

[31] S. Schmid, K. Jensen, K. Nielsen, and A. Boisen, Damping mechanisms in high-Q micro and nanomechanical string resonators, Phys. Rev. B **84**, 165307 (2011).

[32] L. G. Villanueva and S. Schmid, Evidence of Surface Loss as Ubiquitous Limiting Damping Mechanism in SiN Micro- and Nanomechanical Resonators, Phys. Rev. Lett. **113**, 227201 (2014).

[33] M. Rossi, D. Mason, J. Chen, Y. Tsaturyan, and A. Schliesser, Measurement-based quantum control of mechanical motion, Nature **563**, 53 (2018).

[34] G. S. MacCabe, H. Ren, J. Luo, J. D. Cohen, H. Zhou, A. Sipahigil, M. Mirhosseini, and O. Painter, Phononic bandgap nano-acoustic cavity with ultralong phonon lifetime, arXiv:1901.04129 (2019).